Tropical Intraseasonal Variability in the MRI-20km60L AGCM*

PING LIU,[+] YOSHIYUKI KAJIKAWA,[+] BIN WANG,[+] AKIO KITOH,[#] TETSUZO YASUNARI,[@] TIM LI,[+] H. ANNAMALAI,[+] XIOUHUA FU,[+] KAZUYOSHI KIKUCHI,[+] RYO MIZUTA,[&] KAVIRAJAN RAJENDRAN,[**] DUANE E. WALISER,[++] AND DAEHYUN KIM[##]

[+] *International Pacific Research Center, SOEST, University of Hawaii at Manoa, Honolulu, Hawaii*
[#] *Meteorological Research Institute, Tsukuba, Japan*
[@] *Frontier Research Center for Global Change, Japan Agency for Marine-Earth Science and Technology, Kanagawa, Japan*
[&] *Advanced Earth Science and Technology Organization, Meteorological Research Institute, Tsukuba, Japan*
[**] *Centre for Mathematical Modelling and Computer Simulation, National Aerospace Laboratories, Bangalore, India*
[++] *Jet Propulsion Laboratory, California Institute of Technology, Pasadena, California*
[##] *School of Earth and Environmental Science, Seoul National University, Seoul, South Korea*

(Manuscript received 4 January 2008, in final form 22 October 2008)

ABSTRACT

This study documents the detailed characteristics of the tropical intraseasonal variability (TISV) in the MRI-20km60L AGCM that uses a variant of the Arakawa–Schubert cumulus parameterization. Mean states, power spectra, propagation features, leading EOF modes, horizontal and vertical structures, and seasonality associated with the TISV are analyzed. Results show that the model reproduces the mean states in winds realistically and in convection comparable to that of the observations. However, the simulated TISV is less realistic. It shows low amplitudes in convection and low-level winds in the 30–60-day band. Filtered anomalies have standing structures. Power spectra and lag correlation of the signals do not propagate dominantly either in the eastward direction during boreal winter or in the northward direction during boreal summer. A combined EOF (CEOF) analysis shows that winds and convection have a loose coupling that cannot sustain the simulated TISV as realistically as that observed. In the composited mature phase of the simulated MJO, the low-level convergence does not lead convection clearly so that the moisture anomalies do not tilt westward in the vertical, indicating that the low-level convergence does not favor the eastward propagation. The less realistic TISV suggests that the representation of cumulus convection needs to be improved in this model.

1. Introduction

Tropical intraseasonal variability (TISV) exhibits the following two dominant modes: the boreal winter Madden–Julian oscillation (MJO; Madden and Julian 1971, 1972) and the boreal summer intraseasonal oscillations (ISOs; Yasunari 1979; Wang and Rui 1990). These two modes have both distinct and similar characteristics. The MJO exhibits eastward propagation at zonal wavenumbers 1–3 and in a 30–60-day period. Zonal wind anomalies are out of phase in the lower and higher troposphere; they are closely coupled with convection. The coupled pattern initiates in the western Indian Ocean then slowly propagates eastward at a speed of 5 m s^{-1} in the Eastern Hemisphere. Wind anomalies in the atmospheric boundary layer lead in the eastward propagation, building up the moist static energy that fosters deep convection. In contrast, the ISOs have a complex structure exhibiting both eastward and northward propagations (Wang and Rui 1990; Annamalai and Slingo 2001; Lawrence and Webster 2002). The northward migration prevails over the Indian Ocean and in the west Pacific from near the equator to 20°–30°N so as to modulate the Asian summer monsoon at a 30–40-day time scale. Winds and convection associated with the ISO are also closely coupled, moving northward coherently. The MJO–ISO distinction characterizes the TISV seasonality that is attributed to the changes in the background basic state of the atmosphere (Wang 2005).

* School of Ocean and Earth Science and Technology Contribution Number 7574 and International Pacific Research Center Contribution Number 556.

Corresponding author address: Ping Liu, 1680 East-West Road, International Pacific Research Center, University of Hawaii at Manoa, Honolulu, HI 96822.
E-mail: pliu@hawaii.edu

DOI: 10.1175/2008JCLI2406.1

© 2009 American Meteorological Society

General circulation models (GCMs) have great difficulties in simulating the TISV realistically. Early primitive models that had coarse resolution and simple physical processes produced eastward-propagating MJO-like signals that are much faster than those observed (Hayashi and Golder 1986; Lau and Lau 1986). Even the state-of-the-art GCMs with increased resolution and improved physical processes show large deficiencies in capturing the MJO features (Park et al. 1990; Slingo et al. 1996; Wu et al. 2002; Lin et al. 2006). Some models simulated an MJO with a standing structure. Others produced the eastward propagation while the amplitude is too low, the period is too short, or the phase speed is too fast. The modeled coupling between convection and winds is generally weak (Zhang 2005). The simulated ISOs are even less realistic because of their increasing complexity consisting of both northward- and eastward-propagating components (Waliser et al. 2003).

Cumulus convection, which produces latent heat as a primary driving force to the TISV, is represented by parameterization schemes in the GCMs. Because the cumulus has a small spatial scale and short lifetime, in-cloud processes are modeled only crudely because of insufficient observations. As a result, the schemes have a large number of uncertainties, which contributes greatly to the difficulties of the GCMs in simulating the TISV. For example, closure conditions of the schemes contribute differently to the simulated TISV. Slingo et al. (1996) reported that the signal tends to be relatively more realistic in some of the 15 AGCMs that use a closure based on buoyancy than in others that have a closure associated with moisture convergence. However, Lin et al. (2006) suggested that only schemes having a closure linked to moisture convergence could produce relatively better MJO. Using a similar buoyancy-based closure, Zhang and Mu (2005) showed that the simulated MJO is more sensitive to the buoyancy tendency in the free atmosphere than to that in the whole column. In contrast, Sperber and Annamalai (2008) did not find any sensitivity of the simulate ISO to any particular closure.

Cloud-resolving models, which represent the cumulus explicitly, can overcome some fundamental uncertainties in the parameterization schemes. These models thus simulated the TISV more realistically. Ziemiański et al. (2004) embedded a cloud system–revolving model in a 300-km AGCM over the tropical western Pacific. The simulated MJO-like disturbances are much more prominent than in the default model that uses the cumulus scheme only. Miura et al. (2007) reported that an MJO event was realistically simulated by a 7-km global cloud-resolving model using the observed initial conditions. Nonetheless, the cloud-resolving models have such an extraordinarily high resolution that present computing power can afford a simulation of less than 2 months, which is too short to disclose the periodicity and seasonality of the TISV. Conventional AGCMs with increased resolutions and improved cumulus schemes are still necessary for simulating the long-term climate variability associated with the TISV.

The success of the cloud-resolving models suggests that the mesoscale circulations associated with the cumulus convection may be important to the simulated TISV. Gustafson and Weare (2004) supported the importance by showing that a regional model at a 60-km horizontal resolution can improve the simulated MJO, even without intraseasonal perturbations prescribed by the lateral boundary conditions. However, cumulus parameterizations (e.g., Arakawa and Schubert 1974) generally neglect the effect of the mesoscale circulations; this effect can be included by increasing model resolution. A GCM with finer vertical resolution improved the simulated TISV (Inness et al. 2001), but the dependence of the simulated TISV on increasing horizontal resolution is inconsistent. Some models show improvement (Hayashi and Golder 1986), while one reported no effect (Martin 1999) and others even deteriorated the signal (Gualdi et al. 1997; Liess and Bengtsson 2004). Because the horizontal resolution of these models is typically larger than 200 km, a resolution of tens of kilometers is probably necessary to resolve the mesoscale circulations, as in Gustafson and Weare (2004).

In spite of the overall nonsuccess, some GCMs at a 300-km resolution can improve the simulated TISV by using alternative cumulus schemes. Maloney and Hartmann (2001) demonstrated that the relaxed Arakawa and Schubert (1974) scheme improved the variance, periodicity, and eastward propagation of the TISV in the National Center for Atmospheric Research (NCAR) Community Climate Model version 3 (Kiehl et al. 1998). Liu et al. (2005) reported that the Tiedtke (1989) scheme enhanced the MJO disturbances in the NCAR Community Atmospheric Model version 2. The improvements in these two schemes were probably achieved by including more sophisticated cloud processes. For example, a cloud ensemble and different water phases in clouds, rather than a bulk model, are described by the relaxed Arakawa–Schubert scheme. Turbulent effect and vertically variable entrainment are included in the Tiedtke scheme. When these relatively successful schemes are used in a GCM that has a resolution that is high enough to resolve the mesoscale circulations, whether and why the simulated TISV can be improved are the objectives of this study.

An AGCM at a horizontal resolution of T956 (approximately 20 km) and with 60 vertical levels using a variant of

the Arakawa–Schubert scheme has been developed with joint efforts of the Japan Meteorological Agency (JMA) and Meteorological Research Institute (MRI) of Japan; this model is termed the MRI-20km60L AGCM. Earlier, a 10-yr run was carried out using the climatological SST as external forcing. Rajendran et al. (2008) examined the TISV partially in power spectra and eastward propagation in this particular run. They reported that the simulated TISV exhibits eastward propagation in 200-hPa velocity potential, while the power spectra concentrate on periods longer than 90 days. This study continues to investigate the simulated TISV in detail and understand why the simulated TISV is less realistic in a 27-yr Atmospheric Model Intercomparison Project (AMIP; Gates 1992) run using the monthly evolving SST as external forcing. Variance, power spectra, and lag correlation are diagnosed to disclose the modeled TISV features. Following Wheeler and Hendon (2004, hereafter WH04), a composited phase 3 of the MJO is constructed to investigate the simulated convection–circulation interaction. This MJO phase has a convection maximum along the equator near 90°E and a minimum to the west of the date line. Section 2 briefly introduces the model and methodology. Section 3 presents the TISV characteristics and the horizontal and vertical structures of the constructed MJO in phase 3. Section 4 discusses possible causes of the nonsuccess.

2. Model and methodology

a. Model

The MRI-20km60L AGCM is developed for both climate simulation and weather prediction. It is based upon the global numerical weather prediction (NWP) model of the JMA, version JMA-GSM0103, with modifications and improvements. A detailed description of the model can be found in Mizuta et al. (2006); a summary is presented here.

This model uses a spectral transform on the sphere triangularly truncated at 959 waves on 1920 × 960 grid cells (approximately 20 × 20 km^2) and a sigma-pressure hybrid coordinate with 60 vertical levels. The 20-km horizontal resolution is able to resolve the mesoscale circulations associated with the cumulus convection, which is represented by the Arakawa–Schubert scheme with some revisions. The cloud-base mass flux is determined by solving a prognostic equation (Pan and Randall 1998). The upward mass flux has a profile linearly related to height (Moorthi and Suarez 1992). Effects of entrainment and detrainment in downdraft are included between the cloud base and cloud top (Nakagawa and Shimpo 2004), which reduces the cooling bias in the tropical lower troposphere. In addition, clouds are formed prognostically (Smith 1990); cloud amount and cloud water content are statistically estimated (Sommeria and Deardorff 1977). Cloud water is in liquid state above 0°C and in ice state below −15°C; between −15° and 0°C the fraction changes linearly with temperature. A quasi-conservative semi-Lagrangian scheme (Yoshimura and Matsumura 2003) is implemented for stable and efficient time integrations so that the model is able to use a 6-min time step.

The model is forced with monthly SST evolving from 1979 to 2005. Six-hourly outputs are archived, from which daily mean is derived. A two-step box-mean linear interpolation is used to convert the high-resolution data to 1° × 1° then 2.5° × 2.5° for analysis. The December–February (DJF) and June–August (JJA) climatology is derived from the daily output.

b. Methodology

The U.S. Climate Variability and Predictability (CLIVAR) MJO Working Group has developed a standard software package for evaluating both the MJO and ISO in GCMs. The variables in the package include observational datasets of the National Oceanic and Atmospheric Administration (NOAA)-interpolated outgoing longwave radiation (OLR) and the National Centers for Environmental Prediction (NCEP)–NCAR reanalysis (Kalnay et al. 1996) products of 850- and 200-hPa zonal winds at a 2.5° × 2.5° resolution for the period of 1979–2005. Daily anomalies are derived by subtracting the long-term mean. A 20–100-day bandpass filter is then applied to the daily anomalies. Standard metrics, including estimation of variance, power spectra, lag correlation, EOF analysis, and combined EOF (CEOF) analysis, are applied to the filtered series. Apart from these metrics, by incorporating the methods outlined in WH04, modeled anomalies of 200-hPa zonal wind are projected onto the observed first two CEOFs to select events for constructing the horizontal and vertical structure of the MJO in phase 3. Section 3d describes the procedure in detail.

3. Results

a. Mean states

A necessary, but perhaps not a sufficient, condition for GCMs to represent the TISV is the capture of the time-mean climatology in precipitation and zonal wind (Slingo et al. 1996; Wang and Xie 1997; Inness et al. 2003; Jiang et al. 2004). The MRI-20km60L AGCM has simulated realistic mean states in equatorial zonal winds during both the DJF and JJA seasons (Fig. 1). The westerly winds at 850 hPa during DJF (Fig. 1a) over

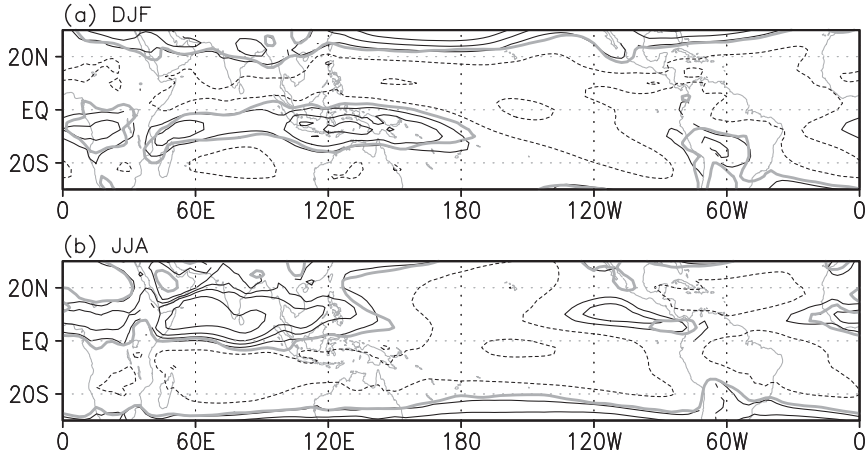

FIG. 1. Long-term-mean (1979–2005) zonal wind at 850 hPa in the MRI-20km60L AGCM for (a) DJF and (b) JJA. Contours are −20, −10, −5, 0, 2.5, 5, 10, and 20 m s^{-1}, with dashed as negative and the first solid line adjacent to a dashed as zero. The thick gray curve corresponds to zero from the NCEP–NCAR reanalysis.

southern equatorial areas in Africa and the Indian Ocean up to the date line is realistically simulated in both spatial range and magnitude compared to the NCEP–NCAR reanalysis. The gray thick curve, which represents the zero line for the reanalysis, mostly coincides with that in the model and extends over the entire southern equatorial areas in the Eastern Hemisphere. The westerly winds in this area are essential for the MJO in eastward propagation (e.g., Slingo et al. 1996; Inness et al. 2003). Many GCMs with coarse resolution, typically 300 km, are able to simulate the westerly winds in only part of the area (e.g., Maloney and Hartmann 2001; Inness et al. 2003).

The zonal wind shear between 200 and 850 hPa from the northern Indian Ocean to the South China Sea traps the equatorial waves in the Asian summer monsoon region, thereby promoting the northward propagation of the ISO mode (e.g., Wang and Xie 1997; Jiang et al. 2004). Here we only show the zonal wind at 850 hPa for clarity; that at 200 hPa has a similarly realistic pattern. As shown in Fig. 1b, the model has produced comparable westerly jets at 850 hPa from Africa to the west Pacific. The simulated zero, indicated by the first solid line adjacent to the dashed line, is collocated with that in the reanalysis (the thick gray line); the modeled westerly winds fall within the same range as the reanalysis in western Africa, the equatorial Indian Ocean, and the western Pacific.

Mean-state OLR in the MRI-20km60L AGCM has a pattern comparable to observations as reported by Rajendran et al. (2008). This is also supported by the two nearly coincident bold contours in Fig. 2 that represent the 230 W m^{-2} of OLR in the NOAA satellite observations (gray) and in the model (black). Nonetheless, differences exist between the model and the observations during DJF and JJA. For example, during DJF (Fig. 2), the model produces somewhat higher OLR, indicating less active convection, over the tropics in Africa, eastern Indian Ocean, and South America. The Indian Ocean, in particular, displays a dipole of ±22 W m^{-2} deficit, indicating more active (suppressed) convection in the west (east). This biased convection dipole also occurs in the composited phase 3 of the model MJO. During JJA (not shown), convection over the Bay of Bengal, Indo-China Peninsula, and South China is weaker than observed, while it is stronger over the central Indian Ocean along 60°E. Such deficiencies in mean OLR correspond to unrealistic TISV features as described below.

b. *Variance, power spectra, and lag correlation*

The climatology in winds and convection are simulated well by the MRI-20km60L AGCM, but the TISV variance (filtered 20–100 day) is much lower than that in the observations. To assess the zonal extent and magnitude of the TISV, in Fig. 3 we show the model-to-observation ratio in the OLR variance. In both seasons, the zonal extent in variance is fairly well captured, but a deficiency in the amplitude is noted. In boreal winter, over the known MJO active regions of the deep tropical (10°S–10°N) Indian and western Pacific Oceans, the ratio is around 0.5, suggesting that the model is only able to produce about 50% of the observed variance. Similarly, in boreal summer (Fig. 3b), about 40%–60% of the variance is simulated in the ISO active regions of the eastern Indian Ocean, South China Sea, and western

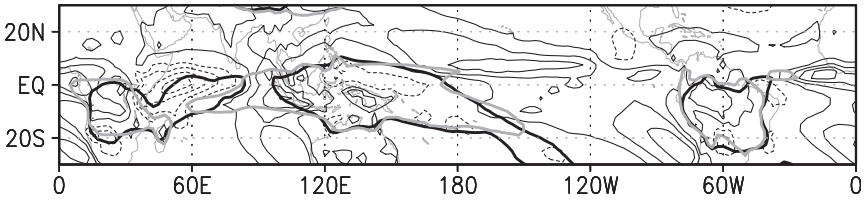

FIG. 2. Long-term-mean (1979–2005) OLR differences between the MRI-20km60L AGCM and the NOAA satellite observations for DJF. Contour interval is 7.5 W m^{-2}, with dashed as negative and zero line omitted. The thick contours correspond to 230 W m^{-2} for the observation (gray) and in the model (black).

Pacific. The simulated 850-hPa zonal wind variance (not shown) also has patterns similar to the observations, but with low amplitudes.

Corresponding to the low variances, the power spectra of the simulated TISV are low. Modeled zonal winds at the upper troposphere have patterns in power spectra in this Atmospheric Model Intercomparison Project (AMIP) run, similar to those in the climatological run reported by Rajendran et al. (2008). The power is prominent at zonal wavenumbers 1–3 during boreal winter, while it is concentrated on time scales greater than 90 days, much longer than the 30–60 days in the observations (not shown). The simulated power spectra in low-level winds are even less realistic. For comparison, Fig. 4a shows the frequency–wavenumber power spectra in the observed 850-hPa zonal wind along the equator averaged between 15°S and 15°N in November–April seasons during 1979–2005. In the observations (Hendon and Salby 1994), the power is concentrated at 30–60 days and at zonal wavenumbers 1–3. Specifically, the central value is above 0.08 m^2 s^{-2} at a 60-day period and at zonal wavenumber 1, which is dominant in the eastward direction. In contrast in the model, although the eastward component at zonal wavenumber 1 dominates (Fig. 4b), the amplitude is substantially lower (0.02 m^2 s^{-2} versus about 0.08 m^2 s^{-2}) and distributed over a wider time scale (30–100 days). The simulated power for westward direction is comparable to the reanalysis but is almost as large as its eastward counterpart, unlike in the observations.

The MJO is weaker during boreal summer (May–October) than winter, which can be shown by the lower power spectra of zonal wind at 850 hPa (Fig. 5a). The power spectra have a central value of 0.05 m^2 s^{-2} in the eastward component, about 60% of which is in winter (cf. Fig. 4a). In contrast, the westward component is nearly 0.01 m^2 s^{-2}, indicating dominant eastward propagation. The difference between power spectra during boreal winter and summer partially characterizes the seasonality of the TISV. The simulated MJO in power spectra in JJA (Fig. 5b), however, is less than 1/5 of that observed in the eastward propagation. The spread is near zonal wavenumber 1 at periods longer than 90 days. Such weak power spectra in both seasons suggest that the model does not

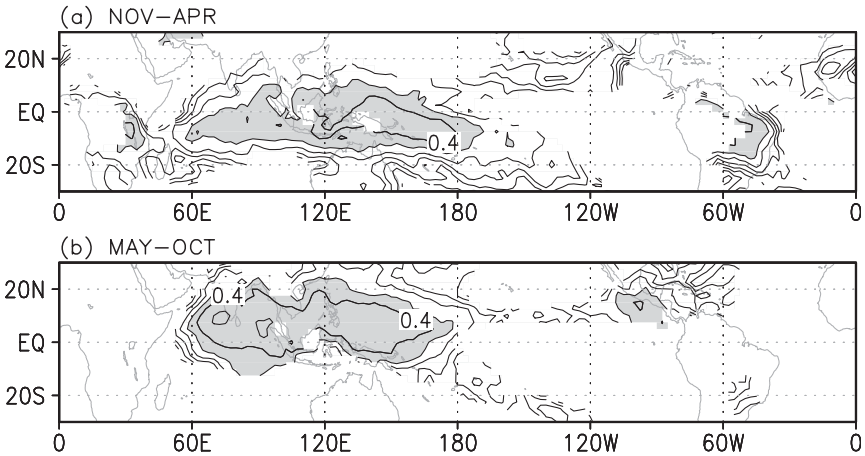

FIG. 3. Model-to-observation ratio of 20–100-day-filtered variance in the NOAA OLR for (a) November–April and (b) May–October averaged in 1979–2005. Model variance less than 150 W^2 m^{-4} is masked out and ratio $\leq$ 0.6 is shaded.

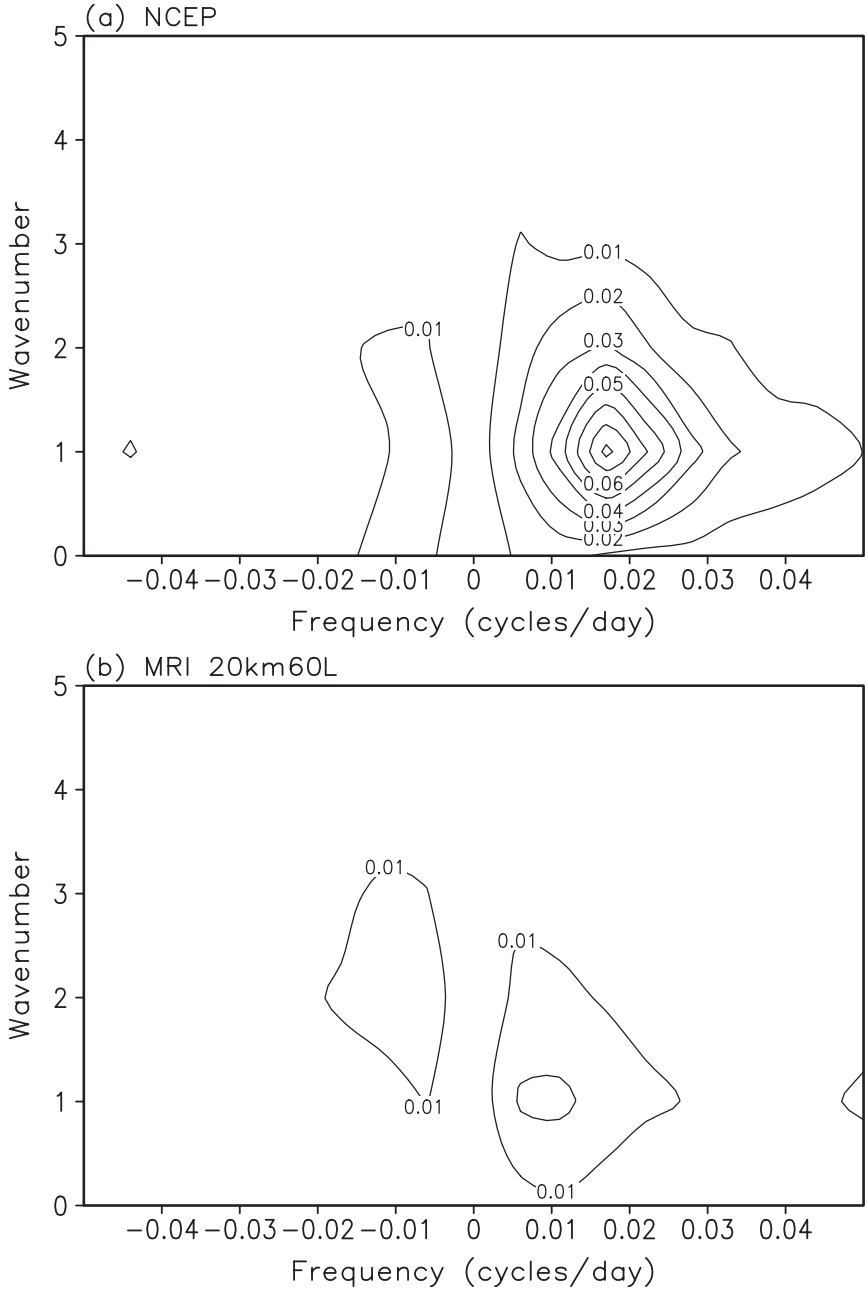

FIG. 4. Frequency–wavenumber power spectra ($m^2 s^{-2}$) of the 850-hPa zonal wind along the equator (15°S–15°N mean) during November–April averaged in 1979–2005 for (a) the reanalysis and (b) the MRI-20km60L model.

realistically reproduce the seasonality of the TISV. The simulated OLR has similarly weak power spectra as the zonal wind at 850 hPa (not shown).

The simulated weak power spectra in zonal winds and convection suggest either the propagating signal is too weak or the signal does not strongly propagate at all. Lag correlation can more clearly disclose either propagating or standing structures. Figure 6a demonstrates the lag correlation of OLR during the November–April season in the observations with the mean of 10°S–10°N on 90°E as the reference point where the OLR has a maximum variance. An eastward-propagating signal starts from day −20 in Africa to the western Indian Ocean, moves slowly eastward at about 5 m s^{-1}, crosses the reference point at day 0, and reaches the date line on the next day −15, showing a 60-day period. The simulated

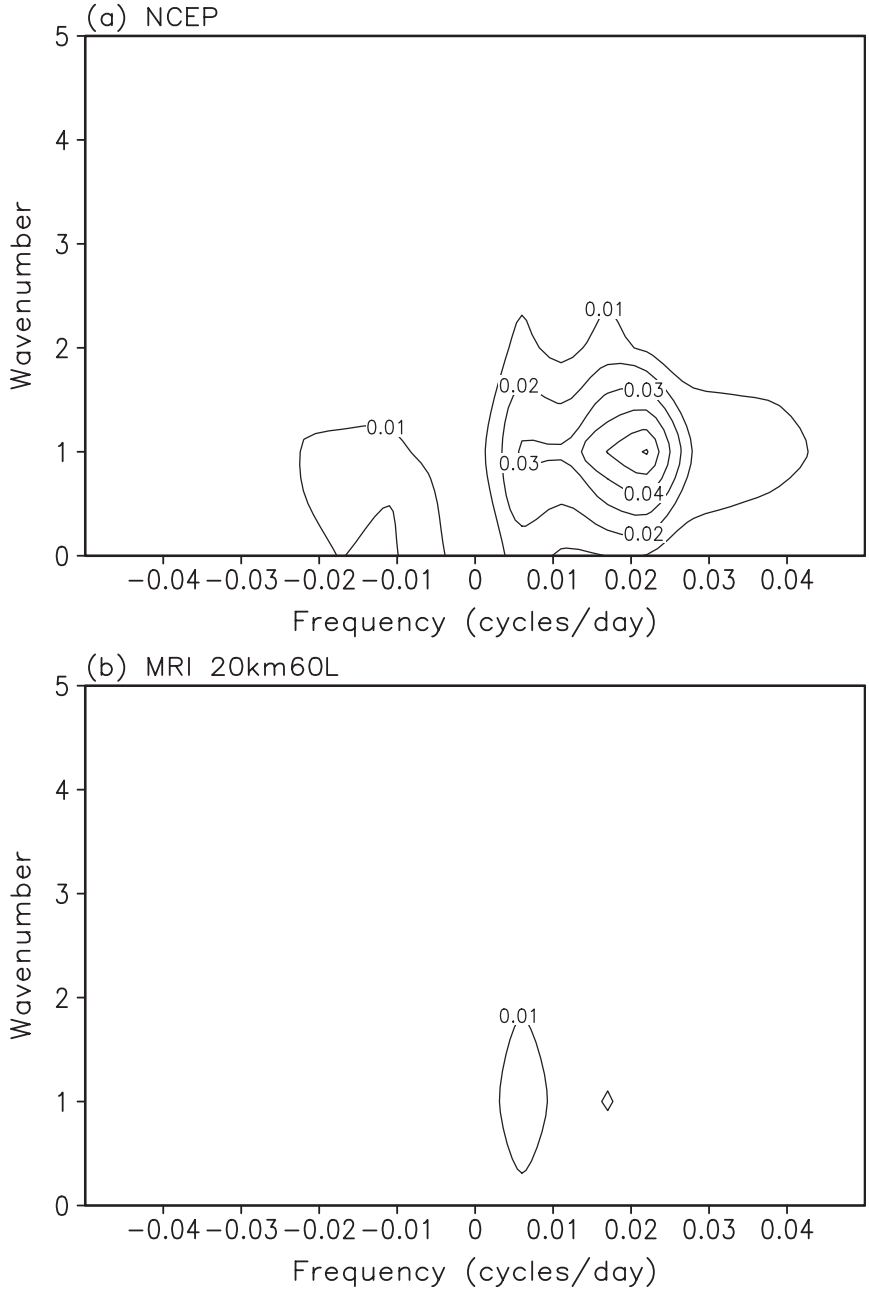

FIG. 5. Same as Fig. 3, but for May–October.

OLR (Fig. 6b), however, has a dominant standing structure centered at 90°E. Isolated moving patches are seen in both eastward and westward directions. In particular, signals in Africa and the western Indian Ocean are completely separated from those of the reference point. This modeled standing structure also occurs in zonal winds at 850 hPa (not shown), although the signals are more connected with the reference in both eastward and westward directions than in OLR. Lag correlation in zonal winds at 200 hPa has more organized eastward propagation features than those in OLR and 850-hPa zonal wind, even though the overall pattern is still less realistic, similar to the climatological run (Rajendran et al. 2008). We will use the relatively better simulated anomalies in 200-hPa zonal wind to derive the MJO events.

The ISO in the observations dominates in the northward propagation separately in the Indian Ocean and in the west Pacific (Yasunari 1979; Wang and Rui 1990). The lag correlation of filtered OLR during May–October in the Indian Ocean sector is shown in Fig. 7, with

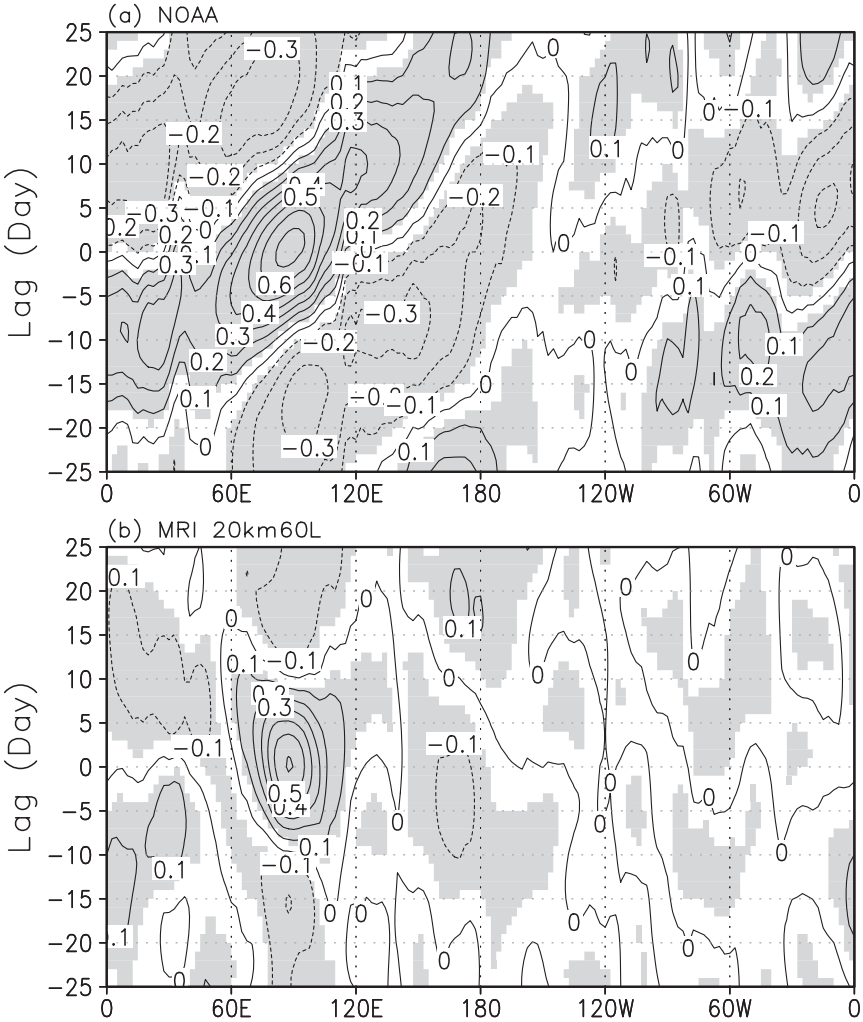

FIG. 6. Lag correlation in OLR along the equator during November–April in 1979–2005 for (a) the NOAA observations and (b) the MRI-20km60L model. Reference point is the mean of 10°S–10°N on 90°E. Shaded values are above 99% significance level.

the equator as the reference point averaged between 80° and 100°E. In the observation (Fig. 7a), the ISO initiates with a suppressed phase just south of the equator on day −25, and then strengthens and matures around day −15. The signal moves in both southward and northward directions. The southward branch reaches 20°S on day −5, which is sooner than the northward branch that reaches 22°N on day 0. The active phase of the oscillation reaches its maxima on day 0 at the equator and also moves in both the southward and northward directions. However, this phase can reach 30°N, much farther northward than the suppressed phase. The active phase decays on the equator near day 10, showing a 35-day period.

The simulated ISO in the Indian Ocean sector (Fig. 7b) oscillates similarly to that in the observations on the equator. A suppressed phase starts on day −25, matures on day −15, and switches to an active phase on day −10. The successive active phase on the equator matures on day 0 and decays on day 10. Thus, the oscillation has a period of 35 days, comparable to that observed. In spite of the similar periodicity, the simulated ISO in the Indian Ocean sector has centers of −0.2 for the suppressed phase and 0.5 for the active, which is weaker than those observed. The northern branches in both suppressed and active phases can only reach 10°N, while the southern branches can propagate as far as 30°S. The main signal is confined within 12°S and 10°N, which is much narrower than that observed, and it has a standing structure.

Observed ISO in the west Pacific sector has distinct features compared to that in the Indian Ocean sector. The lag correlation in Fig. 8 uses a reference point averaged between 115° and 135°E on the equator during

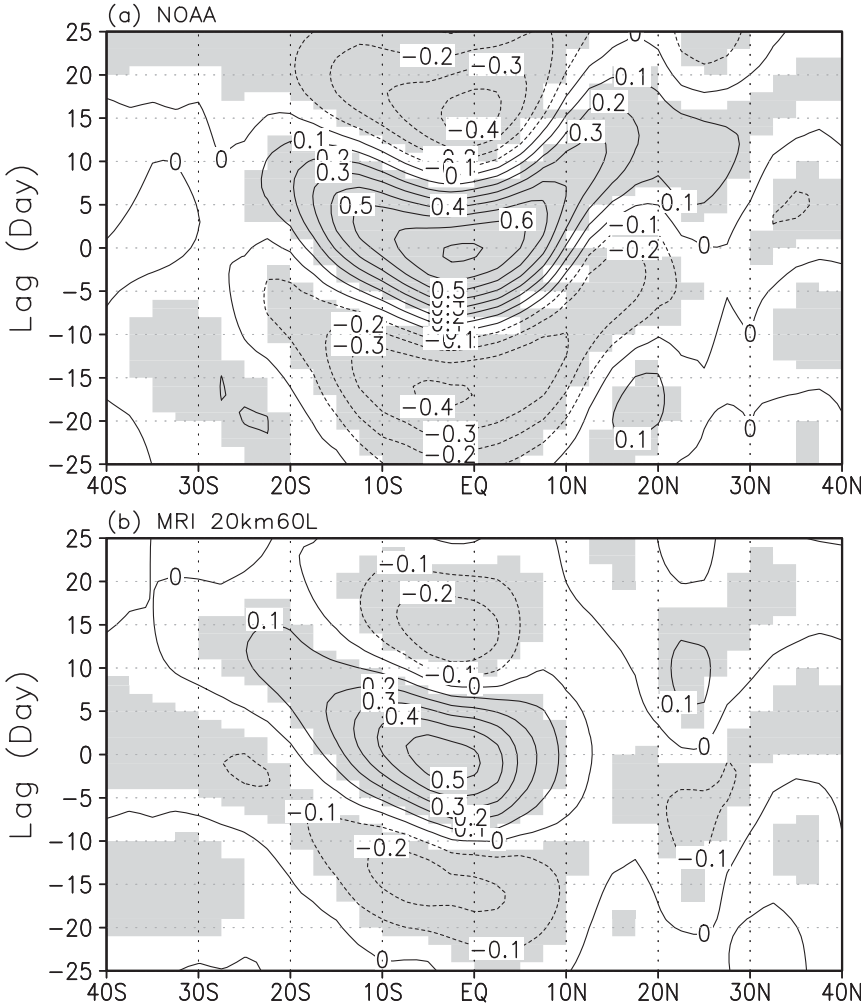

FIG. 7. Lag correlation in OLR during May–October along the Indian Ocean sector for (a) the NOAA observations and (b) the MRI-20km60L model. The reference point is the mean of 80°–100°E on the equator. Shaded values are above 99% significance level.

the May–October season. The observed ISO (Fig. 8a) has a 40-day period on the equator, but its center value is about −0.2 for the suppressed phase and 0.3 for the active phase, which is much weaker than that in the Indian Ocean sector. The oscillation propagates prominently northward and can reach beyond 40°N. The southern branch is predominately a standing feature with lower value during the suppressed phase. During the active phase, north and south signals are separated near 10°S. In this sector at the equator, the simulated ISO (Fig. 8b) starts on day −10 with a suppressed phase, and then switches to an active phase on day 5 and ends on day 20, indicating a period of about 30 days. Minimum and maximum correlation amplitudes, however, are around −0.1 and 0.1, which is about 1/3–1/2 of those observed. The northward part is connected with the southward branch and can reach 30°N, not as far as in the observation. Unlike the relatively static structure in the Indian Ocean sector, the ISO here has discernable northward-propagating features. Because the lag correlation includes all propagating information, an EOF analysis in the following section will effectively isolate the dominant modes of the TISV.

c. *Leading EOFs and the coupled pattern*

EOF analysis has been widely used to separate the phase structures of the TISV from the filtered time series (e.g., Lau and Chan 1985; Knutson and Weickmann 1987; Maloney and Hartmann 1998). Rajendran et al. (2008) applied the extended EOF analysis to the filtered velocity potential at 200 hPa of the 10-yr climatological run from the MRI-20km60L AGCM. They obtained MJO propagating structures similar to that observed, except the spatial scale is smaller. However, when the

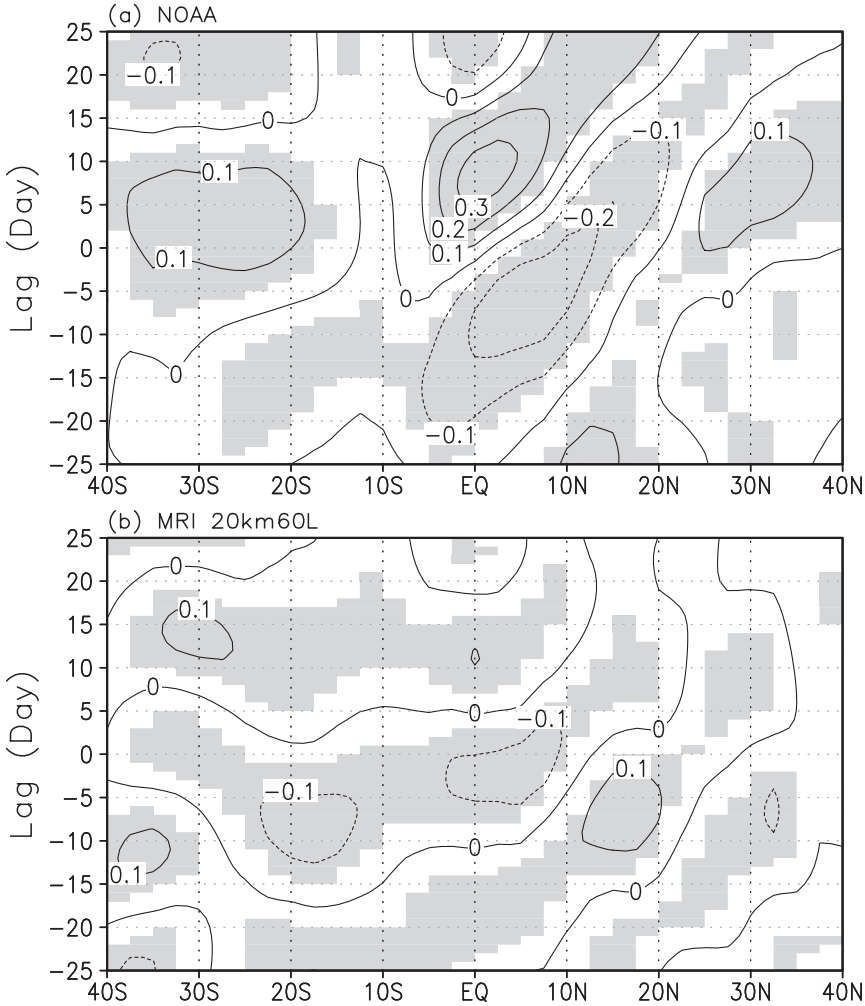

FIG. 8. Same as Fig. 7, but in the west Pacific sector and the reference point is the average between 115° and 135°E on the equator.

EOF analysis is applied to the model OLR and zonal wind at 850 hPa, the leading EOFs demonstrate quite different spatial patterns from those in the observations. Generally, the modeled EOFs have zonally asymmetric structures that are flatter than those observed in convection and winds. The variance of the first two EOFs is too small to separate them from the rest with a statistical significance. These values are listed in Table 1 with the observations for comparison.

The first two EOFs in the observations explain 6.1%–7.6% of the variance in OLR and 9.4%–14.8% of the variance in zonal wind at 850 hPa. Both EOFs are separated from the rest at a significance level with the criterion of North et al. (1982) as disclosed in previous studies (e.g., WH04). The corresponding two EOFs in the model, however, explain 3%–4% of the variance in OLR and 5.5%–6.8% of the variance in zonal wind at 850 hPa, which is about half of that observed. They are very close to the third and fourth EOFs, so they cannot be separated statistically. These inseparable EOFs in both OLR and 850-hPa zonal winds suggest that the coupling among the convection and dynamical fields can be weak, which is demonstrated in a CEOF analysis using OLR and zonal winds at both 850 and 200 hPa.

WH04 tested different combinations of variables for the CEOF analysis optimizing the CEOFs to represent the TISV for real-time monitoring and prediction. They found out that the optimal combination is OLR and 850- and 200-hPa zonal winds, each averaged over the latitudes of 15°S–15°N. They excluded the seasonal mean and ENSO components before analysis without bandpass filtering. The latitude average implicitly filters out small-scale disturbances as indicated in WH04. Here we use the bandpass-filtered data for the CEOF analysis, which produces observed CEOFs almost identical to those in WH04. The two leading CEOFs in the observations are

TABLE 1. Explained variance of the first four leading EOFs either in the observations or in the reanalysis and the MRI-20km60L AGCM. EOF analysis is applied to OLR in 30°N–30°S, 0°–360°, and to zonal wind at 850 hPa in 20°N–20°S, 0°–360°.

	OLR				850-hPa zonal wind			
	NOAA		MRI		Reanalysis		MRI	
	Winter	Summer	Winter	Summer	Winter	Summer	Winter	Summer
EOF 1	7.5%	7.6%	4.1%	3.0%	12.3%	14.8%	6.8%	6.8%
EOF 2	7.2%	6.1%	3.0%	2.8%	9.4%	11.9%	6.1%	5.5%
EOF 3	4.1%	4.2%	2.6%	2.7%	6.3%	5.5%	6.1%	5.3%
EOF 4	3.3%	3.0%	2.5%	2.4%	4.5%	4.8%	4.7%	4.4%

plotted in Fig. 9 for comparison. The first mode (Fig. 9a) starts an active MJO cycle in OLR (solid line) near 60°E, where the 200-hPa zonal wind (short dashed line) is at a negative maximum, while the 850-hPa zonal wind (long dashed line) almost reaches a positive maximum. The winds are in a baroclinic structure and lead convection by about 90° phase. The OLR reaches its maximum at 90°–130°E, where the zonal winds at both 850 and 200 hPa restore back to 0. At 180° longitude, the OLR restores to 0 while the winds almost reach their opposite maxima. The second mode nearly mirrors the first for a suppressed MJO cycle. Both CEOF modes show an apparent quadrature between winds and convection, which is a typical structure of the MJO (e.g., Hendon and Salby 1994). The CEOFs in Fig. 9 coincide with those in WH04 (their Fig. 1), where shorter time series were used, indicating the robustness of the structure.

The two leading CEOFs in the MRI-20km60L AGCM, however, are quite different. In the first mode (Fig. 10a), zonal winds at 850 and 200 hPa have the same sign from 50°–150°E, indicating a barotropic structure rather than a baroclinic structure, as in the reanalysis. Both winds are weak easterly and almost collocated with the OLR from 60° to 120°E, where the observations are separated and in quadrature (Fig. 9a). The OLR amplitude here is barely lower than −0.4, about half of that observed. The second CEOF is also quite different from that in the observations. The simulated OLR has amplitudes between −0.3 and 0.3, which is smaller than that observed. Even though the zonal winds have a baroclinic structure, they are still in phase with the OLR.

Such weak coupling among convection and zonal winds corresponds to the low explained variances by each EOF as listed in Table 2. The first two CEOFs explain about 22% of the variance in the observations, but only 12% in the model. The first two EOFs of the OLR in the model explain only 3%–4% variance, which is much lower than the 13%–15% in the observations. The EOFs for the simulated winds are also lower than those observed. It is noteworthy that the EOFs for the 200-hPa zonal winds have explained a variance almost comparably to observations. This is consistent with the velocity potential at 200 hPa reported by Rajendran et al. (2008). The standard deviations for the OLR and 850- and 200-hPa zonal winds in the model are all smaller than those in the observations. From Figs. 9 and 10, and Tables 1 and 2, the model has simulated generally weak coupled patterns for the TISV.

d. Horizontal and vertical structure of the modeled MJO

The frictional convergence mechanism (Wang 1988) explains why the MJO exhibits eastward propagation. During an MJO life cycle, the convergence in the atmospheric boundary layer is observed to lead in the eastward propagation for building up the moist static energy that fosters the deep convection (Rui and Wang 1990; Hendon and Salby 1994; Maloney and Hartmann 1998). As a result, the anomalous moisture and latent heating have a westward-tilted structure in the vertical with respect to the convection maximum (Sperber 2003; Kiladis et al. 2005). The low-level convergence and vertically westward-tilted pattern associated with the MJO are absent (see Figs. 12 and 13) in the MRI-20km60L AGCM so that the simulated signal has a standing structure.

WH04 derived a TISV index for real-time monitoring and prediction. By projecting the real-time anomalies onto the two leading CEOFs, they derived two principal components as RMM1 and RMM2. A phase map of the RMM1 and RMM2 effectively defines the eight phases of a TISV event. Details about the phase definition can be found in their literature. We next follow their procedure to derive a composited phase 3 of the MJO by projecting the zonal winds at 200 hPa in both the model and the reanalysis onto the observed CEOFs. Because the CEOFs are derived from the 20–100-day bandpass-filtered datasets where components other than the TISV have been excluded, the anomalies used for projection are calculated by simply subtracting climatology from the daily mean. The derived phase 3 of the MJO has a convection maximum in the eastern Indian Ocean and a minimum near the date line as shown by WH04 (their Fig. 5).

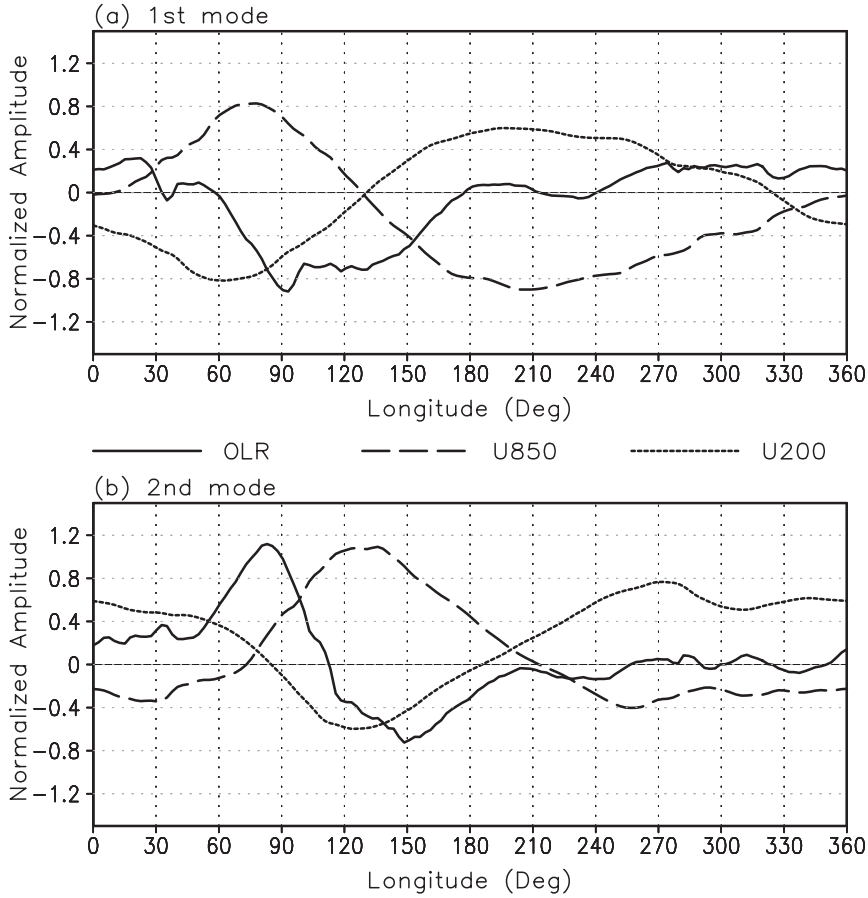

FIG. 9. The first two CEOF modes of 20–100-day filtered 850- and 200-hPa zonal winds and OLR in the observations averaged between 15°N and 15°S from 1979 to 2005.

Figure 11 shows the first two projected principal components RMM1 and RMM2 in the model. Only a few labels are marked for simplicity. The inner circle includes the RMM1 and RMM2 less than one standard deviation. To isolate phases as clearly as possible, we choose points that are over one standard deviation in both the RMM1 and RMM2 to represent the MJO phase 3. These points fall in the small triangle marked with "Ph3." There are about 100 points selected in the model. Using the time indices of these selected events, composites of the OLR, low-level convergence, and vertical structure of the moisture anomalies are derived and shown in Figs. 12 and 13.

Figure 12 shows the composited anomalies of OLR, 850-hPa velocity potential, and divergent wind vectors during the MJO phase 3. The OLR in the observations (shaded in Fig. 12a) clearly displays a dipole structure (cf. Fig. 9b) in the Indian and western Pacific Oceans. The minimum OLR, indicating a maximum convection, is less than -40 W m^{-2} near 90°E. The nonrotated convergence at 850 hPa in the reanalysis, indicated by the solid contours in Fig. 12a, extends from 30°E to 160°W in the 15°S–15°N latitudes, covering the entire tropical Indian Ocean and west Pacific. The convergence center, which is represented by the velocity potential larger than 1×10^7 m^2 s^{-1} and the intersection of divergent easterly and westerly winds, is located near 120°E, about 30° in longitude to the east of the maximum convection. This quadrature pattern indicates that the low-level convergence leads the convection in the eastward propagation. In contrast, Fig. 12b shows the situation in the model. The simulated convection has two maxima in the Indian Ocean, which is different from the one in the observations. The positive 850-hPa velocity potential extends only from 90° to 140°E with values no larger than 2×10^6 m^2 s^{-1}, elucidating a weaker amplitude and narrower range in the simulated low-level convergence than in the reanalysis. This less realistic low-level convergence contributes to a quasi-barotropic vertical structure in the moisture anomalies as shown in Fig. 13.

The thick gray line in Fig. 13 represents the composited OLR anomalies averaged in 15°S–15°N

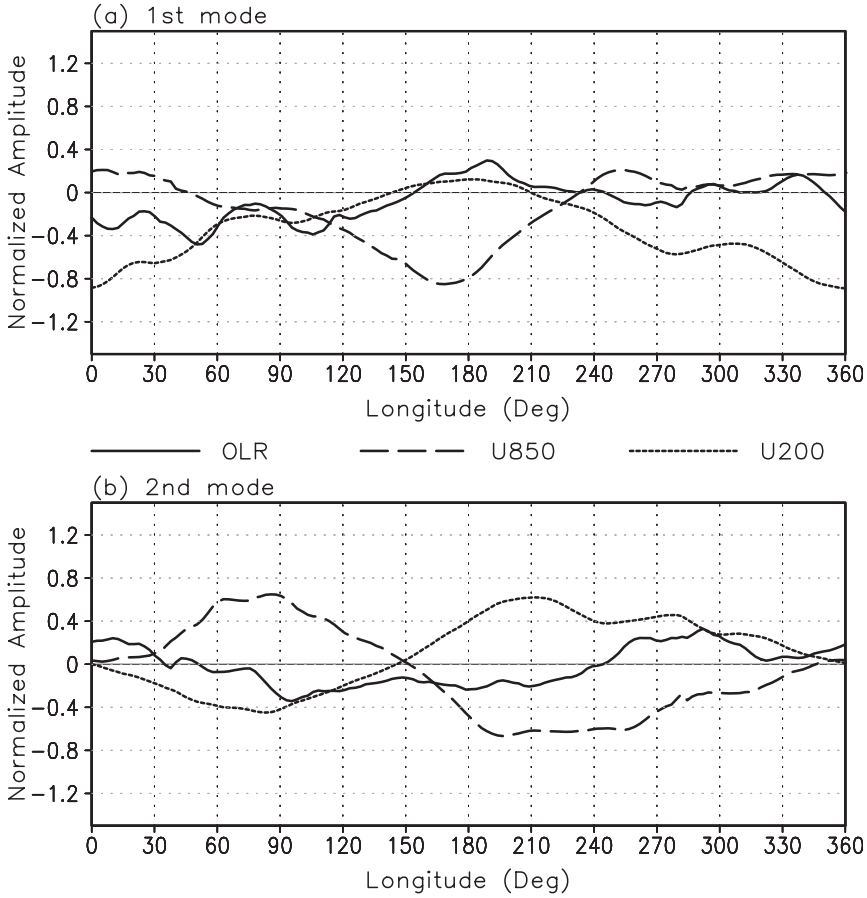

FIG. 10. Same as Fig. 9, but in the MRI-20km60L AGCM.

latitudes in the NOAA observations during this MJO phase. Clearly, a -40 W m^{-2} minimum occurs near 90°E and a 20 W m^{-2} maximum occurs near 180° longitude, which has been shown in Fig. 12a. These two extremes characterize the MJO zonal asymmetry (e.g., Madden and Julian 1971). The modeled OLR (thick black line), however, has two approximately -20 W m^{-2} minima from 30° to 120°E, which is much higher than that in the observations. Corresponding to these minima, the specific humidity anomalies have two positive areas. Interestingly, the one near 30°E lags the OLR minimum at 40°E, while the other at 100°E leads the OLR minimum at 90°E in an eastward direction. The spatial difference between the extremes of the OLR and specific humidity is about 10° in longitude. The extreme of the specific humidity in the observations is clearly in concert with the OLR minimum (Sperber 2003; Kiladis et al. 2005). During the mature phase of the MJO, the moisture anomalies tend to vertically tilt westward with boundary layer moisture, leading convection eastward by about 45° in phase (Sperber 2003; Kiladis et al. 2005). The specific humidity anomalies in Fig. 13 do not show such an apparent westward tilt. This quasi-barotropic structure may explain the

TABLE 2. Explaining variance of the first two leading CEOFs in the observations and the MRI-20km60L AGCM.

	Observation/reanalysis				MRI-20km60L AGCM			
	Total	OLR	U850	U200	Total	OLR	U850	U200
First mode	22.2%	13.2%	31.7%	21.7%	11.9%	3.9%	11.9%	19.9%
Second mode	20.1%	15.9%	23.1%	23.8%	10.8%	3.3%	17.2%	11.9%
Std dev		8.4 W m^{-2}	1.2 m s^{-1}	3.3 m s^{-1}		7.1 W m^{-2}	0.8 m s^{-1}	2.5 m s^{-1}

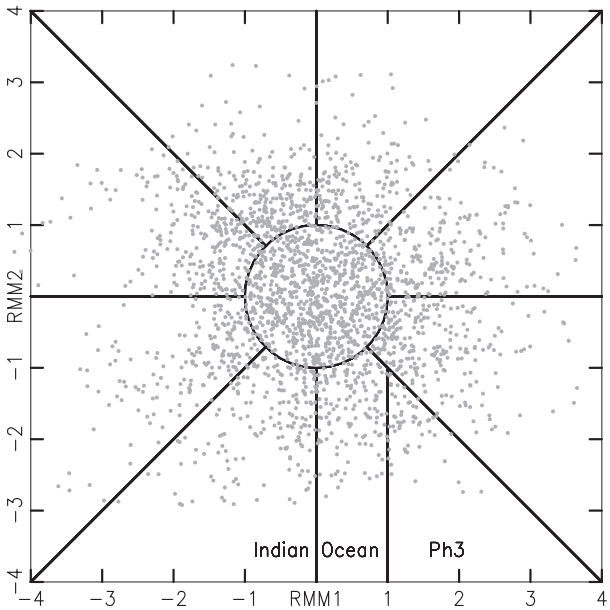

FIG. 11. Phase space of the first two principal components (RMM1 and RMM2) derived by projecting the zonal wind anomalies at 200 hPa in the MRI-20km60L AGCM onto the first two CEOFs in the observations. Each quadrant represents one phase of the MJO with the phase 3 on the right bottom marked by "Ph3". Details about the phase definition can be found in WH04.

standing structure of the MJO as discussed in the lag correlation (Fig. 6).

4. Summary and discussions

The tropical intraseasonal variability is prominent in the observations but is difficult to simulate realistically by the state-of-the-art GCMs. The difficulties are generally attributed to the quality of cumulus parameterization and model resolution, among others. The MRI-20km60L AGCM has very high horizontal and vertical resolution that can resolve the mesoscale circulations associated with the cumulus convection. This model uses a variant of the Arakawa–Schubert scheme that improved the simulated MJO in a 300-km resolution model. Therefore, this AGCM is expected to be able to simulate the salient features of the TISV.

As reported by Rajendran et al. (2008), and further disclosed in this study, however, the model has simulated a TISV with low variance in the 30–60-day band. Power spectra and lag correlation show that the filtered signals have a standing structure, particularly in the eastward-propagating mode during boreal winter. Convection and dynamical fields are coupled too weakly to sustain the TISV. Biased convection in the Indian Ocean corresponds to the standing structure.

It is interesting to note that although the simulated TISV has low variance and standing structures, the simulated background basic states in the atmosphere are comparable to the observations, which are particularly realistic in zonal winds. Previous studies have shown that the realistic basic states are necessary for the initiation and eastward propagation of the TISV. Our results in this model, furthermore, confirm that realistic mean states are not sufficient for a realistic TISV. There are other vital factors that contribute greatly to the model's performance even when the resolution is high enough to resolve the mesoscale circulations associated with the cumulus convection.

One probable factor can be the high ratio of convective to total precipitation. The model convective precipitation occupies nearly 90% of the total in the MJO active areas (Fig. 14). This ratio is much higher than that in the observations. For example, Lin et al. (2004) disclosed that stratiform precipitation can make up to 30%–40% of the total during an MJO event, and Haertel et al. (2008) indicated that the radar-derived stratiform precipitation contributes to the MJO by lagging the convective component for nearly 10 days (their Fig. 18a). Associated with the high ratio, long-term-mean moist diabatic heating along the equator tends to be vertically uniform particularly in the Indian Ocean with a maximum of 4 K day^{-1} near 850 hPa at 60°E, as indicated in Rajendran et al. (2008). This nearly uniform profile is different from the dipole structure as disclosed by Lin et al. (2004), even though that structure occurred in the west Pacific during an MJO event. The actual impact of the vertical heating profile on the simulated TISV, however, will be further investigated.

The weak TISV may suggest that the Arakawa–Schubert cumulus scheme could not be applicable to a model at a 20-km horizontal resolution. A similarly weak and irregular TISV was also simulated in the Soul National University 20-km AGCM implemented with a similar cumulus scheme (I.-S. Kang 2008, personal communication). The Arakawa–Schubert scheme assumes that an area for parameterization should be large enough to host an ensemble of shallow, middle, and deep clouds in a very small fraction with the much larger part for the cloud-free environment. The area-wide processes, for example, advection and surface fluxes, destabilize the column, while the cloud ensemble releases the unstable energy through adjusting the vertical profiles of temperature and moisture in the cloud-free environment. In the MRI-20km60L AGCM, each grid point is configured independently to its neighboring points for the cumulus parameterization. A 20-km grid box can be too small to satisfy the large-area assumption, in particular for the cumulus clusters in hundreds and

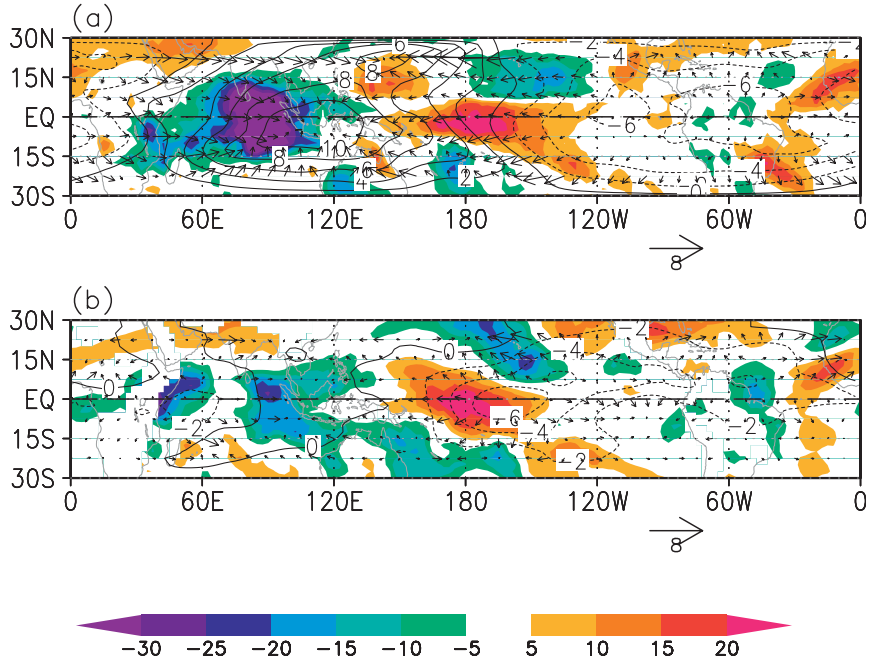

FIG. 12. Composited anomalies of OLR (W m^{-2}; shaded), 850-hPa velocity potential (1×10^6 m^2 s^{-1}; contour), and 850-hPa divergent wind vectors (m s^{-1}) in (a) the NOAA observations and NCEP–NCAR reanalysis and (b) the MRI-20km60L AGCM during phase 3 of the MJO. Phases are selected from the small triangle marked with Ph3 in Fig. 11.

thousands of kilometers scale associated with the TISV. This is probably why the high-resolution version of the Navy Operational Global Atmospheric Prediction System (Peng et al. 2004) replaced the Arakawa–Schubert scheme with the Emanuel (1991) scheme that deals with 100-m scale drafts in cumulus clouds.

Because of the large number of uncertainties in the cumulus schemes, the improvement of the simulated TISV in

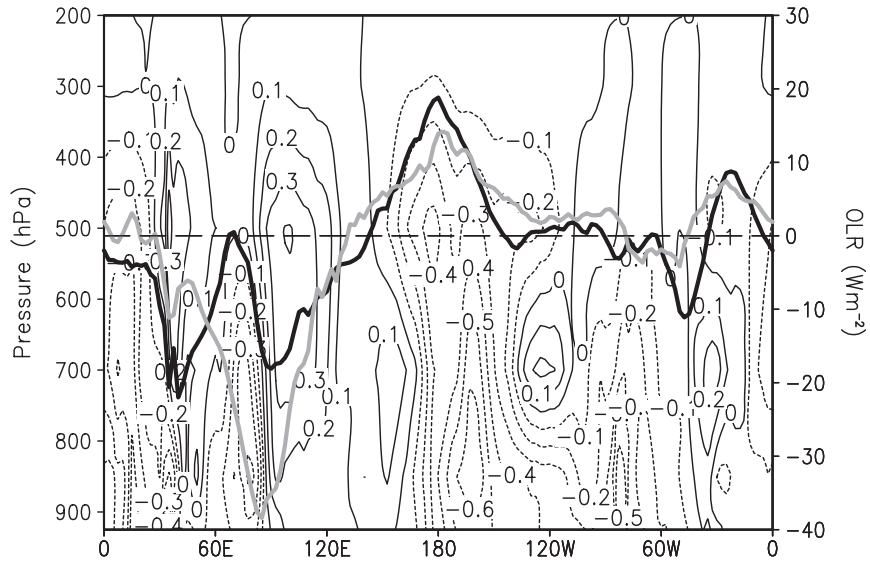

FIG. 13. Vertical structure of the specific humidity (g kg^{-1}) in the composited MJO phase 3. OLR anomalies averaged in 15°S–15°N lats during this phase are plotted in thick lines with black for the model and gray for the NOAA observation.

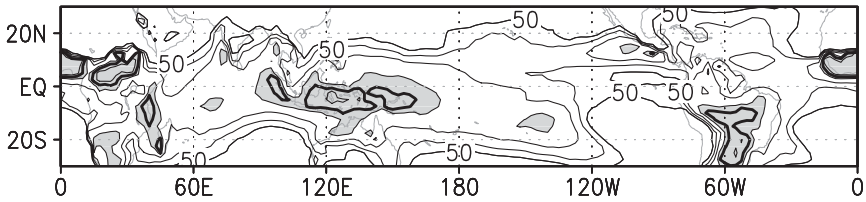

FIG. 14. Ratio in percentile of convective-to-total precipitation during DJF (1979–2005 mean) in the MRI-20km60L AGCM. Values ≥ 50% are contoured with a 10% interval except the 85% (bold) and those ≥80% are shaded.

GCMs has depended greatly on test and trial of different schemes or different features of a specific scheme (e.g., Wang and Schlesinger 1999; Maloney and Hartmann 2001). The Meteorological Research Institute (A. Kitoh 2008, personal communication) is testing the Tiedtke scheme for the TISV simulation in this high-resolution model. Fundamental improvement, however, will come through the improved cumulus schemes in representing the cumulus–circulation interactions using expanded observations and outputs from the cloud-resolving models.

Acknowledgments. This study is supported by the Japan Agency of Marine Science and Technology (JAMESTEC) and NASA Grant NNX07AG53G through their sponsorship of the International Pacific Research Center (IPRC). D. Waliser was supported by the Jet Propulsion Laboratory under a contract with the National Aeronautics and Space Administration. We thank the U.S. CLIVAR MJO Working Group for providing the software package. We also thank Diane Henderson and three reviewers for their comments.

REFERENCES

Annamalai, H., and J. M. Slingo, 2001: Active/break cycles: Diagnosis of the intraseasonal variability of the Asian summer monsoon. *Climate Dyn.,* **18,** 85–102.

Arakawa, O., and W. H. Schubert, 1974: Interaction of cumulus cloud ensemble with the large-scale environment. Part I. *J. Atmos. Sci.,* **31,** 674–701.

Emanuel, K. A., 1991: A scheme for representing cumulus convection in large-scale models. *J. Atmos. Sci.,* **48,** 2313–2335.

Gates, W. L., 1992: AMIP: The Atmospheric Model Intercomparison Project. *Bull. Amer. Meteor. Soc.,* **73,** 1962–1970.

Gualdi, S., A. Navarra, and H. von Storch, 1997: Tropical intraseasonal oscillation appearing in operational analyses and in a family of general circulation models. *J. Atmos. Sci.,* **54,** 1185–1202.

Gustafson, W. I., Jr., and B. C. Weare, 2004: MM5 modeling of the Madden–Julian oscillation in the Indian and west Pacific Oceans: Model description and control run results. *J. Climate,* **17,** 1320–1337.

Haertel, P. T., G. N. Kiladis, A. Denno, and T. M. Rickenbach, 2008: Vertical-mode decompositions of 2-day waves and the Madden–Julian oscillation. *J. Atmos. Sci.,* **65,** 813–833.

Hayashi, Y.-Y., and D. G. Golder, 1986: Tropical intraseasonal oscillation appearing in a GFDL general circulation model and FGGE data. Part I: Phase propagation. *J. Atmos. Sci.,* **43,** 3058–3067.

Hendon, H. H., and M. L. Salby, 1994: The life cycle of the Madden–Julian oscillation. *J. Atmos. Sci.,* **51,** 2225–2237.

Inness, P. M., J. M. Slingo, S. J. Woolnough, R. B. Neale, and V. D. Pope, 2001: Organization of tropical convection in a GCM with varying vertical resolution: Implication for the simulation of the Madden-Julian oscillation. *Climate Dyn.,* **17,** 777–793.

——, ——, E. Guilyardi, and J. Cole, 2003: Simulation of the MJO in a coupled GCM. Part II: The role of the basic state. *J. Climate,* **16,** 365–382.

Jiang, X., T. Li, and B. Wang, 2004: Structures and mechanisms of the northward propagating boreal summer intraseasonal oscillation. *J. Climate,* **17,** 1022–1039.

Kalnay, E., and Coauthors, 1996: The NCEP/NCAR 40-Year Reanalysis Project. *Bull. Amer. Meteor. Soc.,* **77,** 437–471.

Kiehl, J. T., J. J. Hack, G. B. Bonan, B. A. Boville, D. L. Williamson, and P. J. Rasch, 1998: The National Center for Atmospheric Research Community Climate Model: CCM3. *J. Climate,* **11,** 1131–1149.

Kiladis, G. N., K. H. Straub, and P. T. Haertel, 2005: Zonal and vertical structure of the Madden–Julian oscillation. *J. Atmos. Sci.,* **62,** 2790–2809.

Knutson, T. R., and K. M. Weickmann, 1987: 30–60 day atmospheric oscillations: Composite life cycles of convection and circulation anomalies. *Mon. Wea. Rev.,* **115,** 1407–1436.

Lau, K.-M., and P. H. Chan, 1985: Aspects of the 40–50 day oscillation during the northern winter as inferred from outgoing longwave radiation. *Mon. Wea. Rev.,* **113,** 1889–1909.

Lau, N.-C., and K.-M. Lau, 1986: The structure and propagation of intraseasonal oscillations appearing in a GFDL general circulation model. *J. Atmos. Sci.,* **43,** 2023–2047.

Lawrence, D. M., and P. J. Webster, 2002: The boreal summer intraseasonal oscillation: Relationship between northward and eastward movement of convection. *J. Atmos. Sci.,* **59,** 1593–1606.

Liess, S., and L. Bengtsson, 2004: The intraseasonal oscillation in ECHAM4. Part II: Sensitivity studies. *Climate Dyn.,* **22,** 671–688.

Lin, J.-L., B. Mapes, M. Zhang, and M. Newman, 2004: Stratiform precipitation, vertical heating profiles, and the Madden–Julian oscillation. *J. Atmos. Sci.,* **61,** 296–309.

——, and Coauthors, 2006: Tropical intraseasonal variability in 14 IPCC AR4 climate models. Part I: Convective signals. *J. Climate,* **19,** 2665–2690.

Liu, P., B. Wang, K. R. Sperber, T. Li, and G. A. Meehl, 2005: MJO in the NCAR CAM2 with the Tiedtke convective scheme. *J. Climate,* **18,** 3007–3020.

Madden, R. A., and P. R. Julian, 1971: Detection of a 40–50 day oscillation in the zonal wind in the tropical Pacific. *J. Atmos. Sci.,* **28,** 702–708.

——, and ——, 1972: Description of global-scale circulation cells in the tropics with a 40–50 day period. *J. Atmos. Sci.,* **29,** 1109–1123.

Maloney, E. D., and D. L. Hartmann, 1998: Frictional moisture convergence in a composite life cycle of the Madden–Julian oscillation. *J. Climate,* **11,** 2387–2403.

——, and ——, 2001: The sensitivity of intraseasonal variability in the NCAR CCM3 to changes in convective parameterization. *J. Climate,* **14,** 2015–2034.

Martin, G. M., 1999: The simulation of the Asian summer monsoon, and its sensitivity to horizontal resolution, in the UK Meteorological Office Unified Model. *Quart. J. Roy. Meteor. Soc.,* **125,** 1499–1525.

Miura, H., M. Satoh, T. Nasuno, A. T. Noda, and K. Oouchi, 2007: A Madden-Julian oscillation event realistically simulated by a global cloud-resolving model. *Science,* **318,** 1763–1765.

Mizuta, R., and Coauthors, 2006: 20-km-mesh global climate simulations using JMA-GSM model——Mean climate states. *J. Meteor. Soc. Japan,* **84,** 165–185.

Moorthi, S., and M. J. Suarez, 1992: Relaxed Arakawa-Schubert: A parameterization of moist convection for general circulation models. *Mon. Wea. Rev.,* **120,** 978–1002.

Nakagawa, M., and A. Shimpo, 2004: Development of a cumulus parameterization scheme for the operational global model at JMA. *RSMC Tokyo-Typhoon Center Technical Review,* No. 7, Japanese Meteorological Agency, 10–15.

North, G. R., T. L. Bell, R. F. Cahalan, and F. J. Moeng, 1982: Sampling errors in the estimation of empirical orthogonal functions. *Mon. Wea. Rev.,* **110,** 699–706.

Pan, D.-M., and D. Randall, 1998: A cumulus parameterization with a prognostic closure. *Quart. J. Roy. Meteor. Soc.,* **124,** 949–981.

Park, C. K., D. M. Straus, and K. M. Lau, 1990: An evaluation of the structure of tropical intraseasonal oscillation in 3 general circulation models. *J. Meteor. Soc. Japan,* **68,** 403–417.

Peng, M. S., J. A. Ridout, and T. F. Hogan, 2004: Recent modifications of the Emanuel convective scheme in the Navy Operational Global Atmospheric Prediction System. *Mon. Wea. Rev.,* **132,** 1254–1268.

Rajendran, K., A. Kitoh, R. Mizuta, S. Sajani, and T. Nakazawa, 2008: High-resolution simulation of mean convection and its intraseasonal variability over the tropics in MRI/JMA 20-km mesh AGCM. *J. Climate,* **21,** 3722–3739.

Rui, H., and B. Wang, 1990: Development characteristics and dynamic structure of tropical intraseasonal convection anomalies. *J. Atmos. Sci.,* **47,** 357–379.

Slingo, J. M., and Coauthors, 1996: Intraseasonal oscillations in 15 atmospheric general circulation models: Results from an AMIP diagnostic subproject. *Climate Dyn.,* **12,** 325–357.

Smith, R. N. B., 1990: A scheme for predicting layer clouds and their water content in a general circulation model. *Quart. J. Roy. Meteor. Soc.,* **116,** 435–460.

Sommeria, G., and J. W. Deardorff, 1977: Subgrid-scale condensation in models of nonprecipitating clouds. *J. Atmos. Sci.,* **34,** 344–355.

Sperber, K. R., 2003: Propagation and the vertical structure of the Madden–Julian oscillation. *Mon. Wea. Rev.,* **131,** 3018–3037.

——, and H. Annamalai, 2008: Coupled model simulations of boreal summer intraseasonal (30–50 day) variability, Part 1: Systematic errors and caution on use of metrics. *Climate Dyn.,* **31,** 345–372, doi:10.1007/s00382-008-0367-9.

Tiedtke, M., 1989: A comprehensive mass flux scheme for cumulus parameterization in large-scale models. *Mon. Wea. Rev.,* **117,** 1779–1800.

Waliser, D. E., and Coauthors, 2003: AGCM simulations of intraseasonal variability associated with the Asian summer monsoon. *Climate Dyn.,* **21,** 423–446.

Wang, B., 1988: Dynamics of tropical low-frequency waves: An analysis of the moist Kelvin wave. *J. Atmos. Sci.,* **45,** 2051–2065.

——, 2005: Theory. *Intraseasonal Variability in the Atmosphere-Ocean Climate System*, W. K. M. Lau and D. E. Waliser, Eds., Praxis, 307–360.

——, and H. Rui, 1990: Synoptic climatology of transient tropical intraseasonal convection anomalies: 1975-1985. *Meteor. Atmos. Phys.,* **44,** 43–61.

——, and X. Xie, 1997: A model for the boreal summer intraseasonal oscillation. *J. Atmos. Sci.,* **54,** 72–86.

Wang, W. Q., and M. E. Schlesinger, 1999: The dependence on convective parameterization of the tropical intraseasonal oscillation simulated by the UIUC 11-layer atmospheric GCM. *J. Climate,* **12,** 1423–1457.

Wheeler, M. C., and H. H. Hendon, 2004: An all-season real-time multivariate MJO index: Development of an index for monitoring and prediction. *Mon. Wea. Rev.,* **132,** 1917–1932.

Wu, M. L. C., S. Schubert, I.-S. Kang, and D. Waliser, 2002: Forced and free intraseasonal variability over the South Asian monsoon region simulated by 10 AGCMs. *J. Climate,* **15,** 2862–2880.

Yasunari, T., 1979: Cloudiness fluctuation associated with the Northern Hemisphere summer monsoon. *J. Meteor. Soc. Japan,* **57,** 227–242.

Yoshimura, H., and T. Matsumura, 2003: A semi-Lagrangian advection scheme conservative in the vertical direction. *Extended Abstracts, Fifth Int. Workshop on Next Generation Climate Models for Advanced High Performance Computing Facilities,*Rome, Italy, RIST Tokyo, 3.19–3.20. [Available online at http://www.tokyo.rist.or.jp/rist/workshop/rome/abstract/yoshimura.pdf.]

Zhang, C., 2005: Madden-Julian oscillation. *Rev. Geophys.,* **43,** RG2003, doi:10.1029/2004RG000158.

Zhang, G. J., and M. Mu, 2005: Simulation of the Madden–Julian oscillation in the NCAR CCM3 using a revised Zhang–McFarlane convection parameterization scheme. *J. Climate,* **18,** 4046–4064.

Ziemiański, M. Z., W. W. Grabowski, and M. W. Moncrieff, 2004: Explicit convection over the western Pacific warm pool in the Community Atmospheric Model. *J. Climate,* **18,** 1482–1502.

Copyright of Journal of Climate is the property of American Meteorological Society and its content may not be copied or emailed to multiple sites or posted to a listserv without the copyright holder's express written permission. However, users may print, download, or email articles for individual use.